



LAWRENCE  
LIVERMORE  
NATIONAL  
LABORATORY

UCRL-JRNL-206245

# Excitation Cross Section Measurement for $n=3$ to $n=2$ Line Emission in $\text{Fe}^{20+}$ to $\text{Fe}^{23+}$

Hui Chen, Peter Beiersdorfer, Jim Scofield, Greg  
Brown, K.R. Boyce, R. L. Kelley, C. A. Kilbourne, F. S.  
Porter, M. F. Gu, S. M. Kahn

August 26, 2004

Astrophysical Journal

## **Disclaimer**

---

This document was prepared as an account of work sponsored by an agency of the United States Government. Neither the United States Government nor the University of California nor any of their employees, makes any warranty, express or implied, or assumes any legal liability or responsibility for the accuracy, completeness, or usefulness of any information, apparatus, product, or process disclosed, or represents that its use would not infringe privately owned rights. Reference herein to any specific commercial product, process, or service by trade name, trademark, manufacturer, or otherwise, does not necessarily constitute or imply its endorsement, recommendation, or favoring by the United States Government or the University of California. The views and opinions of authors expressed herein do not necessarily state or reflect those of the United States Government or the University of California, and shall not be used for advertising or product endorsement purposes.

# Excitation Cross Section Measurement for $n=3$ to $n=2$ Line Emission in $\text{Fe}^{20+}$ to $\text{Fe}^{23+}$

H. Chen, P. Beiersdorfer, J. H. Scofield,

*High Temperature and Astrophysics Division, Lawrence Livermore National Laboratory, Livermore, CA  
94551*

G.V. Brown <sup>1</sup>

*Department of Physics and Astronomy, The Johns Hopkins University, Baltimore, MD 21218*

K.R. Boyce, R. L. Kelley, C. A. Kilbourne, F. S. Porter

*Goddard Space Flight Center, Greenbelt, MD 20771*

M. F. Gu, S. M. Kahn

*Physics Department, Stanford University, CA 94305*

## ABSTRACT

Electron impact excitation cross sections have been measured for iron L-shell  $3 \rightarrow 2$  lines of Fe XXI to Fe XXIV at the EBIT-II electron beam ion trap using a crystal spectrometer and a  $6 \times 6$ -element array microcalorimeter. The cross sections were determined by direct normalization to the well established cross section of radiative electron capture and a summary of calculated energy dependent radiative recombination cross sections for electron capture into the ground state fine structure levels of  $\text{Fe}^{16+}$  to  $\text{Fe}^{23+}$  ions is given. The measurement results for 17 lines and their comparison with model calculations are presented. While agreement of the model calculations with experiment is good for most measured lines, significant discrepancies were found for a few lines, including the strongest line in Fe XXI.

*Subject headings:* atomic data—line: atomic processes: methods—X-rays: general

---

<sup>1</sup> Also at: Goddard Space Flight Center, Greenbelt, MD 20771

## 1. Introduction

Accurate atomic data are important for the modeling of observed line intensities and for deriving the plasma conditions which are critical in the interpretation of astrophysical observations (Kahn et al. 1990; Paerels & Kahn 2003). Particularly, the atomic data of iron are crucial for interpreting virtually all types of observations since iron is the most abundant high-Z element. As a matter of fact, the spectral-rich iron L-shell has been one of the primary aims of the high-resolution instruments on the *XMM – Newton* and *Chandra* X-ray observatories. Observations with these space crafts are able to resolve many individual spectral features unresolved previously, and they allow for better plasma diagnostics based on these lines. Much theoretical modeling effort has been put forward to interpret these high resolution X-ray spectra. For example, Smith et al. (2001) presented an improved collisional-radiative plasma code APEC that has been widely used in astrophysical data analysis. Also, Behar, Cottam & Kahn (2001) have successfully used the HULLAC atomic code (Bar-Shalom et al. 2001) to model the Capella data obtained using the high-energy transmission grating of *Chandra*. Despite those efforts in improving the atomic calculations, the need for laboratory measurements is clear: repeatedly laboratory data have shown that calculations are incomplete because they miss crucial physics left out as part of the approximations (Beiersdorfer 2003). A prime example is the significant discrepancy found between observations and code predictions, including APEC and HULLAC, in the analysis of Fe XVII and Fe XVIII line ratios (Behar, Cottam & Kahn 2001; Xu et al. 2002). Recent laboratory measurements show that these discrepancies, at least in the case of Fe XVII, are likely due to the accuracy of the excitation cross section of the resonance line (Beiersdorfer et al. 2004; Brown et al. 2004) .

To address the need of validating the calculations using experimental data, our laboratory X-ray astrophysics program, utilizing the electron beam ion traps EBIT-I and EBIT-II at the University of California Lawrence Livermore National Laboratory, has produced large sets of reliable atomic data, including ionization and recombination cross sections for charge balance calculations, emission line lists, excitation cross sections, and dielectronic recombination rates for interpreting X-ray line formation. An overview of this program was given by Beiersdorfer (2003). For iron, we have recently measured a complete set of Fe L-shell emission line wavelengths (Brown et al. 2002, 1998). Various issues associated with the Fe XVII spectrum have been addressed and resolved, including opacity effects, line blending, and cross section measurements (Brown et al. 1998, 2001, 2002, 2004; Beiersdorfer et al. 2002, 2004). Moreover, Gu et al. (1999a, 2001) have reported a set of iron L-shell excitation cross sections for the L-shell lines of Fe XXI–Fe XXIV that were normalized to calculations in the high energy limit. Although such a normalization can be fairly reli-

able at high electron-ion collision energies, the accuracy of electron scattering calculations is limited to 15 – 30% (Zhang et al. 1989), and may be much worse (factors of two or more), if the levels are affected by configuration interactions. A more accurate method is normalizing directly to radiative electron capture, i.e. radiative recombination (RR). This is because RR, the inverse of photoionization, is the simplest atomic scattering process, at high energy involving only one electron and one photon. An RR X-ray is produced by capturing a free electron into a bound level. The X-ray photon has an energy equal to the sum of the free electron energy and the ionization potential of the level into which the electron is captured. At high electron energies, the RR cross sections are known both from calculations and from synchrotron measurements to an accuracy of 3–5% (Saloman et al. 1988).

The first measurement of Fe L-shell cross sections utilizing RR for normalization was reported by Chen et al. (2001). The measurement was made possible in part by the availability of a high-resolution, large area, gain stabilized microcalorimeter, the engineering spare microcalorimeter from the original *ASTRO-E* satellite mission. This instrument had unique characteristics that made such measurement possible, including the ability to time tag each X-ray event and external duty cycle. These measurements of Chen et al. (2001) represented the first use of a calorimeter for cross section measurements. These measurements focused on selected  $n=3 \rightarrow 2$  emission lines of Fe XXIV. In the present, we extend our previous measurement and report the electron impact excitation (EIE) cross sections for 17 lines from the charge states from Fe<sup>20+</sup> to Fe<sup>23+</sup>.

## 2. Experiments

Our experiments were carried out on the EBIT-II device (Levine et al. 1988). In order to measure the Fe L-shell excitation cross section using the RR cross section as normalization, we need a detector that has a wide energy coverage to record not only the EIE (near 1 keV) but also the RR lines (at 4 – 5 keV in this measurement). We also need a detector that has sufficiently high energy resolution to resolve individual EIE line features. This requirement was met by using a crystal spectrometer (Beiersdorfer & Wargelin 1994; Brown et al. 1999) together with the XRS GSFC microcalorimeter detector (Kelley et al. 1999; Stahle et al. 1999; Porter et al. 1999; Audley et al. 1999; Gendreau et al. 1999; Boyce et al. 1999). The microcalorimeter employed in our experiment was the engineering model detector from the *Astro-E* mission (Ogawara et al. 1998). It had an energy resolution better than 10 eV and an energy coverage of about 8.5 keV (500 eV to 9 keV). The crystal spectrometer employed a flat 50 mm  $\times$  25 mm  $\times$  25 mm thallium acid phthalate crystal at a 26 degree Bragg angle, giving a wavelength coverage from 9.5 Å to 12 Å (0.9 – 1.2 keV). It had

a resolving power of 385 (FWHM of 2.6 eV at a photon energy of 1 keV). Typical Fe spectra from both instruments are shown in Fig. 1. The wavelength scale was established by identifying the lines and assigning the line wavelength using references from previous experiments on EBIT-II (Brown et al. 2002) and the PLT tokamak (Wargelin et al. 1998). Most of the Fe  $3 \rightarrow 2$  L-shell lines observed with the crystal spectrometer were resolved, while only a few of those observed with the microcalorimeter were, illustrating the need to operate both instruments simultaneously.

The XRS has unique features that enabled the present measurements. These are a combination of high effective area ( $12.5 \text{ mm}^2$ ), electronic stability, and microsecond-time resolution not yet duplicated in other calorimeter devices. This combination is needed because the RR cross sections are about three orders of magnitude smaller than the electron-impact excitation cross sections. In other words, only one RR X-ray is counted for 1000 counts in a particular L-shell emission line. The microcalorimeter must thus have a large dynamic range, which in an actual measurement translates into a long-time observation without electronic gain drift.

One- and two-times ionized iron was injected into EBIT-II using a metal vapor vacuum arc source. The ions were ionized by the beam and trapped for about five seconds. Then the trap was emptied and filled anew. During the first few hundreds of milliseconds, the injected iron undergoes a step-wise ionization until an equilibrium charge balance is reached, as shown in Fig. 2. We chose to analyze only those data acquired after ionization equilibrium was reached, i.e., data recorded at least one second after the injection.

Our measurements were made at three electron beam energies: 2.1, 2.5, and 3.0 keV. These energies are two to three times higher than the threshold for direct excitation so that we avoid contributions to the line intensities from dielectronic recombination radiation and resonance excitation. At these energies, however, cascades from higher levels may contribute to the line intensities (see section 3.3 for more details). Our method determines the effective cross section that includes all possible cascade processes at the given electron energies.

### 3. Data analysis

EIE cross sections can be derived from the following equation:

$$\sigma = \frac{\sum_j G_j^{RR} \eta_j^{RR} T_j^{RR} \sigma_j^{RR}}{G \eta T} \frac{I}{I_j^{RR}} \quad (1)$$

$\sigma$  is the total cross section for producing the line and includes cascade contributions.  $G$  represents the effects of the angular distribution of the polarized radiation,  $\eta$  is the efficiency of the detector, and  $T$  is the filter transmission. The summation is over the fine structure of a given ion, represented by subscript  $j$ . For example, in the case of electron capture by Li-like Fe XXIV to produce Be-like Fe XXIII, the ground state fine structure includes  $2s_{1/2}^2$  ( $J=0$ ), and  $2s_{1/2}2p_{1/2}$  ( $J=0, J=1$ ),  $2s_{1/2}2p_{3/2}$  ( $J=1, J=2$ ). (A complete list of the fine structure components of the Fe L-shell RR transitions are listed in Table 1.)

It is straightforward to derive the EIE cross sections for each line if we can determine each parameter on the right-hand-side of the equation (1). There is, however, an extra complication in the technique. As illustrated in Fig. 1, the XRS could not fully resolve the  $3 \rightarrow 2$  transition lines. As a consequence, we had to rely on the crystal spectrometer to determine the individual EIE line intensities. To do so we need to relate the line intensities measured with the XRS. We have chosen two Fe XXIV lines  $1s^23p_{1/2} \rightarrow 1s^22s_{1/2}$  and  $1s^23p_{3/2} \rightarrow 1s^22s_{1/2}$ , labeled as Li5 and Li6 in Fig. 1, as common references. These two lines are well isolated from the other lines and their intensities can be determined accurately. The relation between the line intensity measured by the XRS,  $I_X$ , and the one measured by the crystal spectrometer,  $I_c$  is:

$$I_X = A \frac{G_X T_X \eta_X}{G_c T_c \eta_c} I_c \quad (2)$$

The geometry factor  $A$  represents the ratio of the plasma volume in the field of the view of the crystal and the microcalorimeter.

### 3.1. Effect of polarized radiation

Radiation from the electron beam ion trap is excited by a directional electron beam and therefore is polarized (Beiersdorfer et al. 1992; Beiersdorfer & Fujimoto 2001). The measurements reported here were all made by viewing the ions along a line of sight perpendicular to the electron beam. For the measurement with the XRS,  $G = 3/(3 - P)$  for electric-dipole transition, where  $P$  is the degree of linear polarization (Beiersdorfer et al. 1996).  $P$  was calculated using the Flexible Atomic Code (FAC) (Gu 2003), which has a very good agreement with those values calculated using the code of Zhang et al. (1990). For the crystal

spectrometer, factor  $G$  includes not only the effect of the angular distribution of the polarized radiation, but also the crystal reflectivity to the polarized radiation (Beiersdorfer et al. 1992, 1996; Gu et al. 1999a). For the crystal reflectivity, we used a value averaged between perfect and mosaic crystals (Henke, Gullikson, & Davis 1993). We also took into account the depolarizing effect due to a transverse beam energy of 200 eV, following the results of Beiersdorfer et al. (1996) and Gu et al. (1999b).

### 3.2. Detector efficiency

The quantum efficiency of the XRS was obtained prior to the EBIT-II experiments (Gendreau et al. 1999; Audley et al. 1999). The efficiency of the XRS, shown in Fig. 3, consists of foil transmission and detector quantum efficiency. The 5 thin-foil filters are four Al/polyimide filters (each with thickness 545 Å/795 Å, 498 Å/775 Å, 1023 Å/1085 Å, and 1023 Å/1085 Å, respectively) and one 1 μm thick Be foil used to separate the XRS and EBIT-II vacua as well as to reduce the thermal load on the XRS. Also, during the experiment we checked the filter response to look for ice buildup and thus to account for any changes.

The efficiency of the crystal spectrometer was determined by taking into account the photon absorption of the window foils, including a 0.5 μm polyimide window on the spectrometer, and a 1 μm polyimide window on the position sensitive gas proportional counter. Also taken into account was the photon absorption of the P-10 (10% CH<sub>4</sub> and 90% Ar) gas that filled the proportional counter at 1 atmosphere pressure with a depth of 0.9 cm.

### 3.3. RR cross-sections

RR cross sections for photon emission at 90° for each level  $j$  were calculated using a Hartree-Slater model (Scofield 1989, 1991) for all the Fe L-shell ions. This model has been tested and its results have been found to be in good agreement with photoionization experiments (Saloman et al. 1988). From the energy of the levels and the electron beam energy we can determine the position of the RR line, and from the cross sections, we can determine the relative intensity of the lines within one charge state:  $I^{RR} \propto n_i \sigma_j^{RR} v_e$ . As a matter of fact, the accurate knowledge of the relative energy (position) and relative intensity (amplitude) of each RR line provides tight constraints on the RR line intensity fitting (see the following section), and therefore results in an accurate RR line intensity analysis.

To present the theoretical RR cross sections (in unit of  $10^{-24}$  cm<sup>2</sup>), we made a fit to the data at



electron energies (in keV) ranging between 0.5 keV and 10 keV, using a 5th order polynomial fit in  $1/E$ :  $\sigma = a(1/E)^0 + b(1/E)^1 + c(1/E)^2 + d(1/E)^3 + e(1/E)^4 + f(1/E)^5$ . The fitting parameters are listed in Table 1.

### 3.4. RR line intensity

The RR spectra for an electron beam energy of 2.1 keV measured by the XRS microcalorimeter are shown in Fig. 4. The RR X-rays were produced by the capture of beam electrons thereby populating various fine structure levels of the ground states of  $\text{Fe}^{20+}$  through  $\text{Fe}^{23+}$  ions. Unlike in a Maxwellian plasma, RR X-rays excited by a nearly mono-energetic electron beam form distinct, resolved features whose width is determined by the energy distribution of the electron beam. From the data we determine the energy spread of the electron beam to be  $40 \pm 2$  eV for the 2.1 keV electron beam, and  $44 \pm 3$  eV for the 3.0 keV beam. This width is larger than the fine structure separations of the individual RR lines. These separations are as small as 10 eV (see Fig. 4 where the individual RR lines are indicated by thin lines); consequently, we cannot resolve them in the XRS spectrum despite the good resolving power of the microcalorimeter. However, the separations of the RR features among different charge states are typically more than twice the electron beam energy width and can be distinguished clearly in the XRS spectrum.

$I^{RR}$  is determined by fitting the RR emission using the relative position and relative intensities of each RR fine structure configuration known from theory (see Table 1.) We achieved very reliable spectral fits for the RR spectra at all three beam energies.

It is interesting to note that we have different charge balances in the trap at these three electron energies, and this information can be extracted from the RR intensities. We can infer the ionization balance from spectral fits to the RR data using:

$$n_i \propto \frac{I^{RR}}{\sum_j G_j^{RR} \eta_j^{RR} T_j^{RR} \sigma_j^{RR}} \quad (3)$$

The results are in Table 2 for the beam energies of 2.1, 2.5 and 3.0 keV. The dominant ion in the trap was Fe XXIII at an electron beam energy of 2.1 keV, while Fe XXIV and Fe XXV ions became dominant at an electron beam energy of 3.0 keV. This charge balance information was used for the excitation line fitting process as described in next section.

### 3.5. EIE line intensity

The complexity of the Fe L-shell spectrum requires a line fitting procedure that takes into account all possible lines, because many weak lines could have a non-negligible contribution to the intensity of strong lines. To account for all possible line features, we constructed a model utilizing the data from the Fe L-shell line survey (Brown et al. 2002). The model includes all observed L-shell emission lines with measured wavelengths and relative intensities at all charge states. From the charge balance obtained through the RR line fitting (Table 2), we derived initial amplitudes for each line using the available relative intensities of lines from each individual charge states (Brown et al. 2002). During fitting, we allowed the relative intensity to vary within 30% to account for unmeasured factors such as polarization effects. The position of the lines were fixed. The line shape was fit by a Voigt profile, which is a convolution of a Lorentzian and Gaussian function. The line width was set to be the same for all the lines. This information provided us with a constraint similar to that of the RR line fitting discussed above. As is shown in Fig. 5, we achieved good fits to the measured spectra using this constrained method.

We noticed that the fitting of a couple of lines could be improved, if we would set the line wavelength as a free parameter. For example, the intensity of the C-like Fe XXI line C10 would increase between 10%-30% if its wavelength was allowed to vary from 12.284 Å (1.009 keV) up to 12.312 Å (1.007 keV). Such a wavelength variation, however, would be inconsistent with the data from the wavelength survey (Brown et al. 2002). Moreover, there is a possibility that the few lines that appear to be imperfectly fitted could be blended by unidentified weak lines. We note that even a change by 30% would not remove the discrepancies between some experimental and theoretical results, as discussed below.

The data used for the EIE fitting are summarized in Table 3, where the line labels, transition energies and relative line intensities are taken from Brown et al. (2002).

## 4. Results and discussions

The results of the EIE cross section measurements for the lines from Fe XXI to Fe XXIV are summarized in Table 4. The error analysis included the statistical fitting error of the line intensities as well as uncertainties in filter transmissions and detector responses for both the crystal spectrometer and the microcalorimeter. We also estimated the errors associated with accounting for the angular distribution correction and crystal reflectivities. An additional error comes from determining the appropriate intensity of the background level,

given the high density of the unresolved weak iron lines in the XRS spectra. In the analysis, we estimated the upper and lower limit of the background level to assess this error. The total error given is from the quadrature summation of all individual errors.

In Table 4, the EIE cross sections from the present measurement are compared with the theoretical values of the EIE cross sections from calculations utilizing the codes FAC (Gu 2003) and HULLAC (Bar-Shalom et al. 2001). A graphical comparison for selected lines is shown in Fig. 6. At the present electron energies, levels higher than  $n=3$  can be excited, and cascades from such higher- $n$  levels contribute to the observed line intensities. In the FAC calculations, cascades from up to  $n = 12$  are included, and up to  $n = 6$  are included in the HULLAC calculations. Overall, the cascade contribution account for 4% to 50% of the total line intensities, as shown in Table 5. We expect cascade contributions from  $n > 12$  to be negligible.

Our measurements show that the calculations are in good agreement with many of the measurements for B-like, Be-like and Li-like lines. This indicates that the calculations are quite accurate in many cases. However, some significant discrepancies exist.

Firstly, the measured cross sections for the Li5 and Li6 lines are slightly lower than those calculated, particularly at the electron energy of 2.1 keV. These observation are consistent with our previous measurements for those lines (Chen et al. 2001), where the measured cross sections were somewhat lower compared to R-matrix calculations. The physical cause of this discrepancy is not clear. We note that cascades from levels up to  $n=12$  have been taken into account in our calculations. However, cascades will only add to the theoretical value which is already larger than the measurement. The differences between our measurements and calculations are largest at the lowest energy. While the calculated cross sections diminish with electron energy, the measured cross sections for Li5 and Li6 seem rather constant. By contrast, the measured cross sections for Li1, Li3 and Li4 decrease with electron energy as predicted by the calculations.

Secondly, the calculated cross section of the Be-like Fe XXII line Be1 also appears to be somewhat larger than the measurement. For example the measured value is  $6.4 \pm 0.6 \times 10^{-21} \text{ cm}^2$  at the 2.1 keV electron energy, which is about 25% less than the calculated values of  $8.7 \times 10^{-21} \text{ cm}^2$  (FAC) and  $8.6 \times 10^{-21} \text{ cm}^2$  (HULLAC). This line (Be1) is blended with the B6 line B-like Fe XXII (Brown et al. 2002), and therefore we might have incorrectly accounted for the line blend although we have used the tightest available constraints. Indeed, our results for line B6 are somewhat larger than the calculated values, albeit the discrepancy is within the uncertainty limit of the measurement. However, even if some of the cross section of line B6 was assigned to Be1, it would be insufficient to bring the measured cross section of Be1 into agreement with the

calculations. A similarly blended line pair is formed by lines B13 and Be2. Here good agreement is found between measurement and calculation. We note that line Fe XXII B13 ( $1s^2 2s^2 3d_{3/2} J=3/2 \rightarrow 1s^2 2s^2 2p_{1/2} J=1/2$ ) is sensitive to the plasma density (Wargelin et al. 1998; Chen et al. 2004). Although this property could potentially affect the measurement, it was not the case in our measurements. At densities between  $1 \times 10^{10} \text{cm}^{-3} - 1 \times 10^{12} \text{cm}^{-3}$ , the EBIT-II source is at the low density limit for this line.

Thirdly, the relatively small population of C-like ions in the trap resulted in larger uncertainties in the measurements for C-like lines than for the lines of the other charge states. The increased uncertainties, however, cannot explain the large discrepancy (almost a factor of 2) between measurement and theory for the strongest line Fe XXI C10. As discussed before, the intensity of this line could be increased by up to 30% if we allowed its wavelength to be a variable in our fit. Such a relaxation of the fit constraints is not enough to reduce the large observed discrepancy and would not resolve the discrepancy. One possible explanation is the density sensitivity of this line  $1s^2 2s^2 2p_{1/2} 3d_{3/2} J=1 \rightarrow 1s^2 2s^2 2p^2 J=0$ , which starts at densities of about  $10^{11} \text{cm}^{-3} - 10^{12} \text{cm}^{-3}$  (Phillips et al. 1996). At these densities, which are close to those estimated for our machine, the population in the ground state fine structure levels  $1s^2 2s^2 2p^2 J=1$  and  $J=2$  become sufficiently high so that the excitation from the ground level  $J=0$  will be reduced, resulting in a lower measured cross section. However, the predicted reduction is still too little to account for the measured results.

We expect that further measurements and improved modeling will eventually resolve the discrepancies noted for the few lines in Fe XXI, Fe XXIII and Fe XXIV. Until these discrepancies are resolved we recommend not to use these lines for determining abundances and other parameters when analyzing astrophysical spectra, especially when other lines from these ionization stages are available for diagnostic purposes.

This work was performed under the auspices of the U.S. Department of Energy by the University of California Lawrence Livermore National Laboratory under contract No. W-7405-Eng-48 and supported by NASA Astronomy and Physics Research and Analysis grants to LLNL, GSFC, and Stanford University.

## REFERENCES

- Audley, M. D., et al, 1999, SPIE 3765, 751
- Bar-Shalom, A., Klapisch, M., & Oreg, J. 2001, J. Quant. Spec. Radiat. Transf., 71, 169
- Behar, E., Cottam, J., & Kahn, S. M., 2001, ApJ, 548, 966

- Beiersdorfer, P., Phillips, T. W., Wong, K. L., Marrs, R. E., & Vogel, D. A., 1992, *Phys. Rev. A*, 46, 3812
- Beiersdorfer, P. & Wargelin, B. J., 1994, *Rev. Sci. Instrum.* 65, 13
- Beiersdorfer, P., et al, 1996, *Phys. Rev. A* 53, 3974
- Beiersdorfer, P., et al, 1999, *PRA* 60, 4156
- Beiersdorfer, P., et al, 2002, *ApJ* 576, L169
- Beiersdorfer, P. & Fujimoto, T., 2001, *Proceedings for the 3rd Plasma Polarization Spectroscopy workshop*, Livermore, California, UCRL-ID-146907
- Beiersdorfer, P., 2003, *Annu. Rev. Astron. Astrophys.*, 41, 343
- Beiersdorfer, P., et al, 2004, *ApJ*, 610, 616
- Boyce, K. R., et al, 1999, *SPIE* 3765, 741
- Brown, G. V., Beiersdorfer, P., Liedahl, D. A., Widmann, K., Kahn, S. M. & Clothiaux, E. J., 2002, *ApJS*, 140, 589
- Brown, G. V., Beiersdorfer, P., Chen, H., Chen, M. H. & Reed, K. J., 2001, *ApJ*, 557, L75
- Brown, G. V., Beiersdorfer, P., Liedahl, D. A., Widmann, K. & Kahn, S. M. 1998, *ApJ*, 502, 1015
- Brown, G. V., Beiersdorfer, P., Widmann, K., 1999, *Rev. Sci. Instrum.* 70, 280
- Brown, G. V., Beiersdorfer, P., et al., 2004, in preparation.
- Chantrenne, S., Beiersdorfer, P., Cauble, R., & Schneider, M. B., 1992, *Phys. Rev. Lett.* 69, 265
- Chen, H., Beiersdorfer, P., Scofield, J. H., Gendreau, K. C., Boyce, K. R., Brown, G. V., Kelley, R. L., Porter, F. S., Stahle, C. K., Szymkowiak, A. E., & Kahn, S. M., 2002, *ApJ* 567, L169
- Chen, H., Beiersdorfer, P., Heeter, L. A., Liedahl, D. A., Naranjo-Rivera, K. L., Träbert, E., Gu, M. F. & Lepson, J. K. 2004, *ApJ*, to appear in August issue
- Gendreau, K. C., et al, 1999, *SPIE* 3765, 137
- Gu, M. F., Kahn, S. M., Savin, D. W., Beiersdorfer, P., Liedahl, Brown, G. V., Reed, K. J., Bhalla, C. P., & Grabbe, S. R., 1999a, *APJ*, 518, 1002

- Gu, M. F., Savin, D. W., & Beiersdorfer, P., 1999b, *J. Phys. B*, 32, 5371
- Gu, M. F., Kahn, S. M., Savin, D. W., Bahar, E., Beiersdorfer, P., Brown, G. V., Liedahl & Reed, K., 2001, *ApJ*, 563, 462
- Gu, M. F., 2003, *ApJ*, 582, 1241
- Henke, B. L., Gullikson, E. M., & Davis, J. C. 1993, *At. Data Nucl. Data Tables*, 54, 181
- Kahn, S. M., & Liedahl, D. A., 1990, in *Iron Line Diagnostics in X-ray Sources*, edited by A. Treves, G. C. Perola & L. Stella, Springer-Verlag, p3
- Paerels, F. B. S. & Kahn, S. M., 2003, *Ann. Rev. Astron. Astrophys.*, 41, 291
- Phillips, K. J. H., Bhatia, A. K., Mason, H. E., & Zarro, D. M., 1996, *ApJ*, 466, 549
- Kelley, R. L., et al, 1999, *SPIE*, 3765, 114
- Levine, M. A., Marrs, R. E., Henderson, J. R., Knapp, D. A., & Schneider, M. B., 1988, *Physics Scripta*, T22, 157
- Ogawara, Y. 1998, *Proc. of IAU Symp. No. 188 Kyoto*
- Porter, F. S., et al, 1999, *SPIE* 3765, 729
- Porter, F. S., et al, 2000, *SPIE* 4140, 407
- Saloman, E. B., Hubbell, J. H., & Scofield, J. H., 1988 *At. Data Nucl. Data Tables* 38, 1
- Scofield, J. H. 1989, *Phys. Rev. A*, 40, 3054
- Scofield, J. H. 1991, *Phys. Rev. A*, 44, 139
- Smith, R. K., Brickhouse, N. S., Liedahl, D. A., & Raymond, J. C., 2001, *ApJ*, 556, L91
- Stahle, C. K., et al, 1999, *SPIE* 3765, 82
- Wargelin, B. J., Beiersdorfer, P., Liedahl, D. A., Kahn, S. M., & von Goeler, S., 1998, *ApJ* 496, 1031
- Xu, H., Kahn, S. M., Peterson, J. R., et al., 2002, *ApJ* 579, 600
- Zhang, H. L. & Sampson, D. H., 1989, *Atomic Data and Nuclear Data Tables*, 43, 1
- Zhang, H. L., Sampson, D. H., & Clark, R. E. H., 1990, *Phys. Rev. A*, 41, 198



Table 1: Fit parameters for the theoretical total cross section of RR transitions (in units of  $10^{-24}\text{cm}^2$ ) into ground state fine structure L-shell levels.

Index	Structure	Binding energy	Fitting parameters					
		eV	$a$	$b$	$c$	$d$	$e$	$f$
Fe XXIV	$2s_{1/2}J = 1/2$	2046	-11.246	256.630	120.343	-134.196	64.849	-11.477
Fe XXIV	$2p_{1/2}J = 1/2$	1997	-1.025	-1.272	342.710	-260.136	102.948	-16.196
Fe XXIV	$2p_{3/2}J = 3/2$	1981	-1.703	-7.414	670.755	-506.274	199.805	-31.397
Fe XXIII	$2s_{1/2}2s_{1/2}J = 0$	1951	-5.590	125.475	59.147	-68.937	33.887	-6.056
Fe XXIII	$2s_{1/2}2p_{1/2}J = 0$	1908	-0.207	-1.101	87.725	-65.667	25.745	-4.025
Fe XXIII	$2s_{1/2}2p_{1/2}J = 1$	1904	-0.607	-3.543	261.808	-195.746	76.675	-11.978
Fe XXIII	$2s_{1/2}2p_{3/2}J = 2$	1892	-0.849	-8.154	428.865	-319.023	124.652	-19.453
Fe XXIII	$2s_{1/2}2p_{3/2}J = 1$	1855	-0.566	-3.959	254.884	-190.871	74.837	-11.698
Fe XXIII	$2p_{1/2}2p_{1/2}J = 0$	1832	-0.023	0.629	0.583	-0.730	0.379	-0.071
Fe XXIII	$2p_{3/2}2p_{3/2}J = 0$	1772	-0.214	5.003	1.967	-2.545	1.296	-0.235
Fe XXII	$2p_{1/2}J = 1/2$	1800	-0.646	-7.564	363.570	-269.323	104.790	-16.295
Fe XXII	$2p_{3/2}J = 3/2$	1785	-0.944	-19.778	711.219	-523.565	203.110	-31.550
Fe XXI	$2p_{1/2}2p_{1/2}J = 0$	1688	-0.279	-3.788	166.241	-124.785	48.871	-7.629
Fe XXI	$2p_{1/2}2p_{3/2}J = 1$	1679	-0.342	-8.123	273.985	-203.701	79.257	-12.314
Fe XXI	$2p_{1/2}2p_{3/2}J = 2$	1674	-0.485	-10.634	367.592	-273.369	106.411	-16.542
Fe XXI	$2p_{3/2}2p_{3/2}J = 2$	1658	-0.119	-2.494	87.312	-65.214	25.463	-3.967
Fe XXI	$2p_{3/2}2p_{3/2}J = 0$	1637	-0.044	-0.325	19.703	-14.752	5.742	-0.890
Fe XX	$2p_{3/2}J = 3/2$	1572	-0.397	-13.749	408.734	-302.912	117.589	-18.246
Fe XX	$2p_{1/2}2p_{3/2}2p_{3/2}J = 3/2$	1554	-0.300	-8.980	277.541	-206.063	79.990	-12.401
Fe XX	$2p_{1/2}2p_{3/2}2p_{3/2}J = 1/2$	1536	-0.058	-0.970	39.130	-29.408	11.482	-1.784
Fe XX	$2p_{3/2}J = 3/2$	1529	-0.003	-0.080	2.653	-1.974	0.771	-0.120
Fe XIX	$2p_{3/2}2p_{3/2}J = 2$	1454	-0.295	-12.756	358.971	-266.294	103.276	-16.008
Fe XIX	$2p_{3/2}2p_{3/2}J = 0$	1444	-0.052	-2.354	64.762	-47.835	18.471	-2.852
Fe XIX	$2p_{1/2}2p_{3/2}(3)J = 1$	1443	-0.084	-4.347	117.896	-87.691	34.083	-5.292
Fe XIX	$2p_{1/2}2p_{3/2}(3)J = 2$	1433	0.000	-0.204	5.128	-3.917	1.555	-0.246
Fe XVIII	$2p_{3/2}J = 3/2$	1352	-0.146	-14.267	346.643	-255.437	98.435	-15.179
Fe XVIII	$2p_{1/2}J = 1/2$	1339	-0.006	-0.679	16.182	-11.960	4.613	-0.711



Table 2: Relative charge abundance in the electron beam ion trap inferred from microcalorimeter measurements of L-shell radiative recombination photons.

Ions	2.1 keV	2.5 keV	3.0 keV
Fe XXV	0.04	0.32	0.44
Fe XXIV	0.26	0.38	0.36
Fe XXIII	0.39	0.22	0.14
Fe XII	0.23	0.08	0.04
Fe XXI	0.08	-	0.03

Table 3: Emission line wavelength and relative intensity used in the EIE fitting program.

Label	Atomic transition	Wavelength Å	Energy eV	Rel. Intensity
C4	$1s^2 2s_{1/2} 2p_{1/2} 2p_{3/2} 3d_{5/2} J = 2 \rightarrow 1s^2 2s_{1/2} 2p^2 2p_{3/2} J = 1$	12.822	0.967	0.5
C5	$1s^2 2s_{1/2} 2p_{1/2} 2p_{3/2} 3d_{5/2} J = 2 \rightarrow 1s^2 2s_{1/2} 2p_{1/2} 2p_{3/2}^2 J = 1$	12.649	0.980	0.1
C6	$1s^2 2s^2 2p_{1/2} 3d_{5/2} J = 3 \rightarrow 1s^2 2s^2 2p_{1/2} 2p_{3/2} J = 2$	12.499	0.992	0.2
C7	$1s^2 2s^2 2p_{1/2} 3d_{5/2} J = 2 \rightarrow 1s^2 2s^2 2p_{1/2} 2p_{3/2} J = 1$	12.422	0.998	0.1
C8	$1s^2 2s^2 2p_{1/2} 3d_{3/2} J = 1 \rightarrow 1s^2 2s^2 2p_{1/2} 2p_{3/2} J = 1$	12.393	1.000	0.2
C9	$1s^2 2s^2 2p_{3/2} 3d_{5/2} J = 2, 3 \rightarrow 1s^2 2s^2 2p_{1/2} 2p_{3/2} J = 2$	12.327	1.006	0.1
C10	$1s^2 2s^2 2p_{1/2} 3d_{3/2} J = 1 \rightarrow 1s^2 2s^2 2p^2 J = 0$	12.284	1.009	1
C11	$1s^2 2s_{1/2} 2p_{1/2} 2p_{3/2} 3d_{3/2} J = 2 \rightarrow 1s^2 2s_{1/2} 2p_{1/2}^2 2p_{3/2} J = 1$	12.204	1.016	0.1
C12	$1s^2 2s_{1/2} 2p_{1/2} 2p_{3/2} 3p_{3/2} J = 1 \rightarrow 1s^2 2s^2 2p_{1/2} 2p_{3/2} J = 1$	12.044	1.029	0.05
C13	$1s^2 2s_{1/2} 2p^2 3p_{3/2} J = 1 \rightarrow 1s^2 2s^2 2p^2 J = 0$	11.975	1.035	0.1
B4	$1s^2 2s_{1/2} 2p_{1/2} 3s_{1/2} J = 1/2 \rightarrow 1s^2 2s_{1/2} 2p_{1/2} 2p_{3/2} J = 3/2$	12.754	0.972	0.3
B5	$1s^2 2s_{1/2} 2p_{1/2} 3d_{5/2} \rightarrow 1s^2 2s_{1/2} 2p_{1/2} 2p_{3/2} J = 3/2$	12.210	1.015	0.4
B6	$1s^2 2s_{1/2} 2p_{3/2} 3d_{5/2} \rightarrow 1s^2 2s_{1/2} 2p_{1/2} 2p_{3/2} J = 3/2$	12.144	1.021	0.1
B7	$1s^2 2s_{1/2} 2p_{3/2} 3d_{5/2} \rightarrow 1s^2 2s_{1/2} 2p_{3/2}^2 J = 3/2$	12.089	1.026	0.1
B8	$1s^2 2s_{1/2} 2p_{3/2} 3d_{3/2} \rightarrow 1s^2 2s_{1/2} 2p_{3/2}^2 J = 3/2$	12.038	1.030	0.1
B9	$1s^2 2s^2 3d_{3/2} J = 3/2 \rightarrow 1s^2 2s^2 2p_{3/2} J = 3/2$	11.977	1.035	0.2
B10	$1s^2 2s^2 3d_{5/2} J = 5/2 \rightarrow 1s^2 2s^2 2p_{3/2} J = 3/2$	11.932	1.039	0.4
B11	$1s^2 2s_{1/2} 2p_{1/2} 3d_{5/2} J = 5/2 \rightarrow 1s^2 2s_{1/2} 2p_{1/2} 2p_{3/2} J = 3/2$	11.881	1.044	0.2
B12	$1s^2 2s_{1/2} 2p_{1/2} 3d_{5/2} J = 5/2 \rightarrow 1s^2 2s_{1/2} 2p_{1/2} 2p_{3/2} J = 3/2$	11.802	1.051	0.2
B12	$1s^2 2s_{1/2} 2p_{3/2} 3d_{3/2} J = 3/2 \rightarrow 1s^2 2s_{1/2} 2p^2 J = 1/2$			
B13	$1s^2 2s^2 3d_{3/2} J = 3/2 \rightarrow 1s^2 2s^2 2p_{1/2} J = 1/2$	11.770	1.053	1
B14	$1s^2 2s_{1/2} 2p_{1/2} 3p_{3/2} J = 3/2 \rightarrow 1s^2 2s^2 2p_{3/2} J = 3/2$	11.704	1.059	0.05
B15	$1s^2 2s_{1/2} 2p_{1/2} 3p_{1/2} J = 1/2 \rightarrow 1s^2 2s^2 2p_{1/2} J = 1/2$	11.640	1.065	0.05
B16	$1s^2 2s_{1/2} 2p_{1/2} 3p_{1/2} J = 1/2 \rightarrow 1s^2 2s^2 2p_{1/2} J = 1/2$	11.578	1.071	0.05
B17	$1s^2 2s_{1/2} 2p_{3/2} 3p_{1/2} J = 1/2 \rightarrow 1s^2 2s^2 2p_{3/2} J = 3/2$	11.530	1.075	0.05
B18	$1s^2 2s_{1/2} 2p_{1/2} 3p_{3/2} J = 3/2 \rightarrow 1s^2 2s^2 2p_{1/2} J = 1/2$	11.490	1.079	0.2
B19	$1s^2 2s_{1/2} 2p_{1/2} 3p_{3/2} J = 3/2 \rightarrow 1s^2 2s^2 2p_{1/2} J = 1/2$	11.427	1.085	0.2
B20	$1s^2 2s_{1/2} 2p_{3/2} 3p_{3/2} J = 3/2 \rightarrow 1s^2 2s^2 2p_{3/2} J = 3/2$	11.400	1.088	0.05

Table 3. Continue

Label	Atomic transition	Wavelength Å	Energy eV	Rel. Intensity
Be1	$1s^2 2s_{1/2} 3s_{1/2} J = 0 \rightarrow 1s^2 2s_{1/2} 2p_{3/2} J = 1$	12.161	1.020	0.3
Be2	$1s^2 2s_{1/2} 3d_{5/2} J = 2 \rightarrow 1s^2 2s_{1/2} 2p_{3/2} J = 1$	11.736	1.056	1
Be3	$1s^2 2s_{1/2} 3s_{1/2} J = 1 \rightarrow 1s^2 2s_{1/2} 2p_{1/2} J = 1$	11.702	1.060	0.1
Be3	$1s^2 2p_{1/2} 3d_{5/2} J = 3 \rightarrow 1s^2 2p_{1/2} 2p_{3/2} J = 2$			
Be4	$1s^2 2s_{1/2} 3d_{5/2} J = 3 \rightarrow 1s^2 2s_{1/2} 2p_{3/2} J = 2$	11.458	1.082	0.07
Be5	$1s^2 2s_{1/2} 3d_{3/2} J = 1 \rightarrow 1s^2 2s_{1/2} 2p_{1/2} J = 1$	11.366	1.091	0.05
Be6	$1s^2 2s_{1/2} 3d_{3/2} J = 2 \rightarrow 1s^2 2s_{1/2} 2p_{1/2} J = 1$	11.336	1.094	0.05
Be7	$1s^2 2s_{1/2} 3d_{3/2} J = 1 \rightarrow 1s^2 2s_{1/2} 2p_{1/2} J = 0$	11.285	1.099	0.05
Be8	$1s^2 2s_{1/2} 3p_{1/2} J = 1 \rightarrow 1s^2 2s^2 J = 0$	11.019	1.125	0.39
Be9	$1s^2 2s_{1/2} 3p_{3/2} J = 1 \rightarrow 1s^2 2s^2 J = 0$	10.981	1.129	0.6
Li1	$1s^2 3s_{1/2} J = 1/2 \rightarrow 1s^2 2p_{3/2} J = 3/2$	11.432	1.085	0.4
Li2	$1s^2 3s_{1/2} J = 1/2 \rightarrow 1s^2 2p_{1/2} J = 1/2$	11.266	1.101	0.15
Li3	$1s^2 3d_{5/2} J = 5/2 \rightarrow 1s^2 2p_{3/2} J = 3/2$	11.176	1.109	1
Li4	$1s^2 3d_{3/2} J = 3/2 \rightarrow 1s^2 2p_{1/2} J = 1/2$	11.029	1.124	0.5
Li5	$1s^2 3p_{1/2} J = 1/2 \rightarrow 1s^2 2s_{1/2} J = 1/2$	10.663	1.163	0.4
Li6	$1s^2 3p_{3/2} J = 3/2 \rightarrow 1s^2 2s_{1/2} J = 1/2$	10.618	1.168	0.8

Table 4: Results of excitation cross sections (in units of  $10^{-21}\text{cm}^2$ ) at three electron beam energies from this experiment and two theoretical models. The values in parentheses represent the uncertainties of the measured values.

Line	2.1keV			2.5keV			3.0keV		
	Measurement	FAC	HULLAC	Measurement	FAC	HULLAC	Measurement	FAC	HULLAC
C4	5.7 ( 1.0 )	4.9					7.1 ( 2.9 )	4.2	
C8	4.3 ( 0.9 )	5.6					4 ( 1.5 )	4.9	
C10	16.3 ( 3.3 )	32.3	32.9				11.2 ( 3.2 )	28.6	32
B6	2.5 ( 0.6 )	1.9		2.3 ( 0.8 )	1.8		2.3 ( 0.6 )	1.6	
B10	4.4 ( 0.8 )	5.2					4.2 ( 0.8 )	3.9	
B13	15.9 ( 2.5 )	17.4	17.8	11.5 ( 2.1 )	16.2	17.2	13.9 ( 2.3 )	15	16
B19	3.4 ( 0.6 )	3.2	4.1	2.6 ( 0.6 )	3.2	3.6	3.6 ( 0.7 )	3.1	3.4
Be1	6.4 ( 0.6 )	8.7	8.6	5.7 ( 0.8 )	7.6	7.1	5.1 ( 0.6 )	6.6	6.1
Be2	15.8 ( 1.4 )	15.7	15.9	11.4 ( 1.6 )	14.7	14.1	12.8 ( 1.5 )	13.4	13.1
Be4	1.2 ( 0.2 )	1.6		0.8 ( 0.2 )	1		0.8 ( 0.1 )	0.6	
Be8	4.4 ( 0.4 )	4.3	4.3	4.1 ( 0.6 )	4.1	4.1	4.2 ( 0.5 )	4	4.2
Be9	6.4 ( 0.6 )	6.6	6.4	6.2 ( 0.9 )	6.6	6.1	6.8 ( 0.8 )	6.4	6.4
Li1	3.4 ( 0.3 )	3.4	3.3	2.7 ( 0.4 )	2.9	2.6	2.3 ( 0.2 )	2.5	2.2
Li3	7.1 ( 0.6 )	6.4	6.8	5.2 ( 0.6 )	5.6	5.7	5.3 ( 0.5 )	4.9	5.2
Li4	3.7 ( 0.3 )	3.6	3.4	3 ( 0.4 )	3.1	3	2.9 ( 0.3 )	2.7	2.8
Li5	1.8 ( 0.2 )	2.4	2.3	2 ( 0.3 )	2.3	2	2.1 ( 0.2 )	2.1	2.1
Li6	3.5 ( 0.3 )	4.5	4	4.1 ( 0.5 )	4.3	3.9	3.6 ( 0.4 )	4.1	3.7

Table 5: Calculated cascade contribution to the line intensity at an electron collision energy of 2.4 keV using code FAC.

Line	Fraction
C4	0.085
C8	0.11
C10	0.04
B6	0.36
B10	0.25
B13	0.05
B19	0.18
Be1	0.05
Be2	0.09
Be4	0.52
Be8	0.17
Be9	0.19
Li1	0.11
Li3	0.134
Li4	0.14
Li5	0.18
Li6	0.19

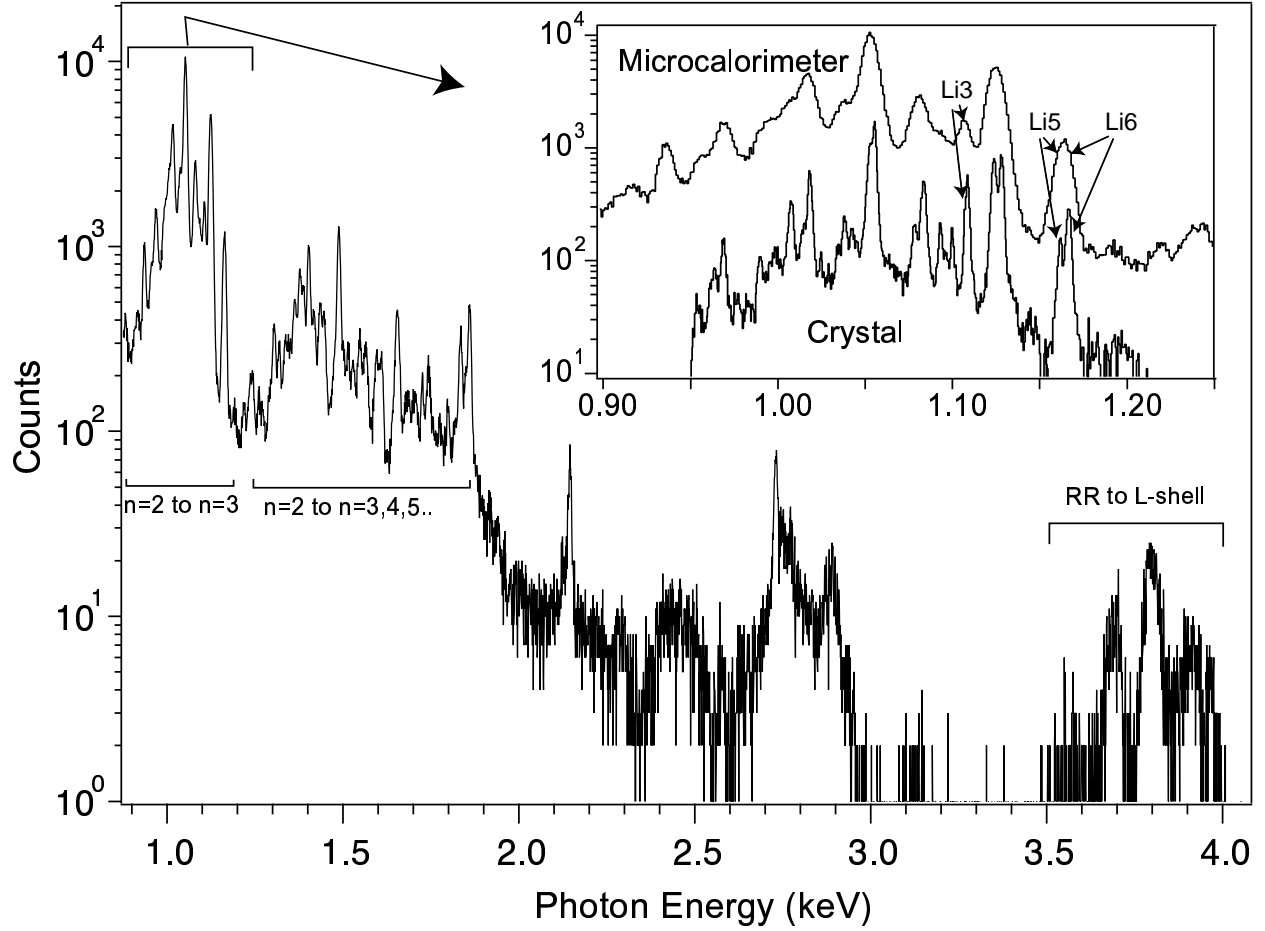


Fig. 1.— Iron spectrum taken by the XRS microcalorimeter at an electron beam energy of 2.1 keV. The insert is an enlarged view of the  $3 \rightarrow 2$  lines from both the XRS and the TlAP crystal spectrometer. The line width of the L-shell lines reflects the resolution of microcalorimeter or crystal spectrometer while the line width of the RR lines is due to the energy distribution of the electron beam.

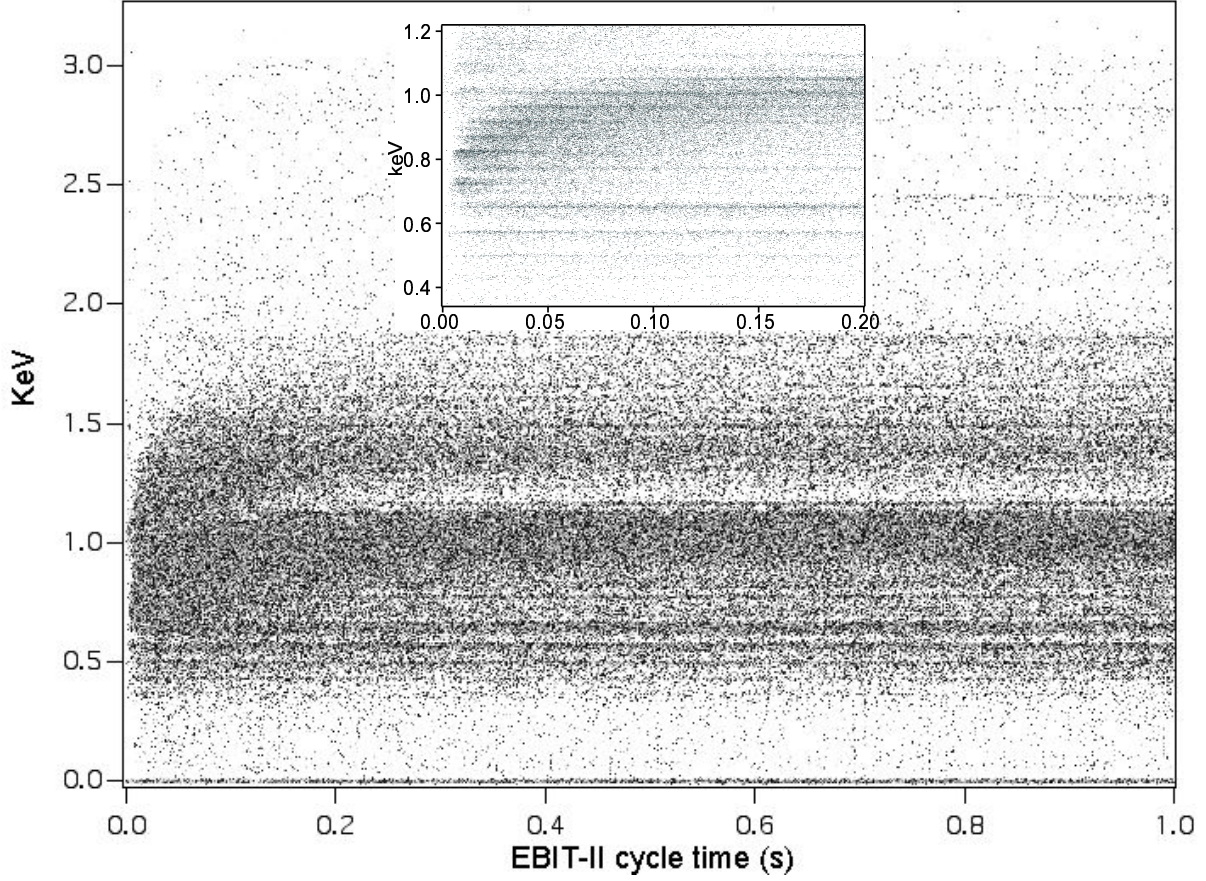


Fig. 2.— The first second of XRS Fe spectrum as a function of EBIT phase time at an electron energy of 2.1 keV. The Fe was injected at 0 s. The ionizing phase lasted until up to 300 ms and is indicated by a successive shift in the observed X-ray energies to higher energies, as shown in the inserted figure for the first 200 ms. The total trapping time was 5 s.

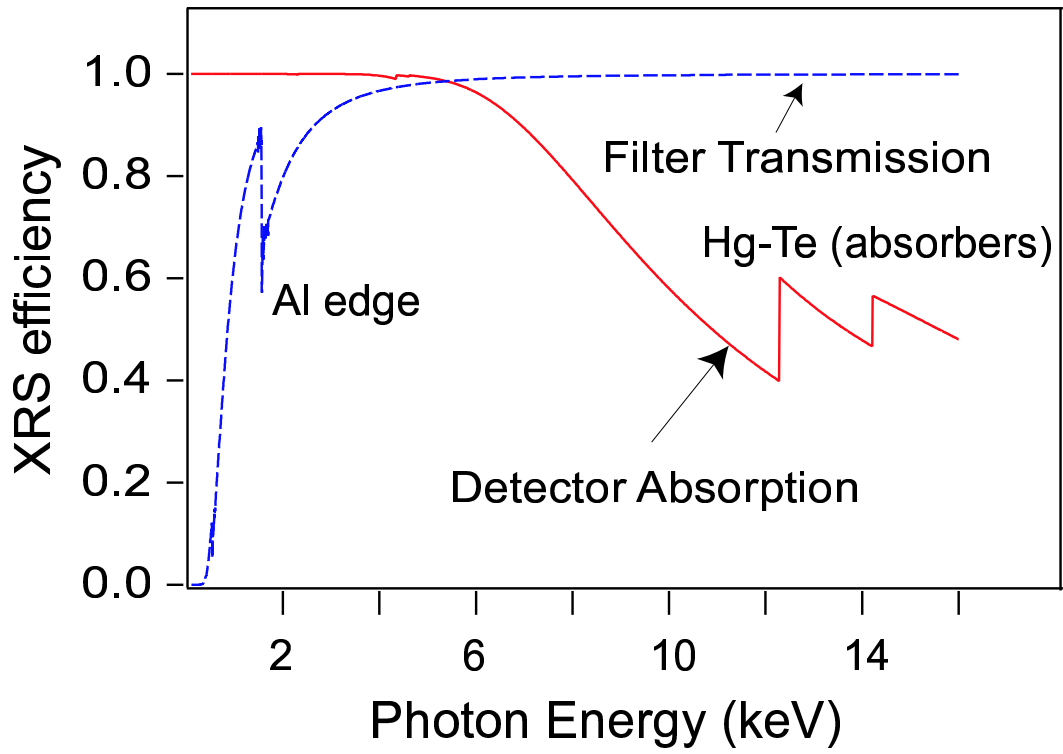


Fig. 3.— The measured transmission efficiency of the window foils and the absorption efficiency of the absorber of the XRS detector.



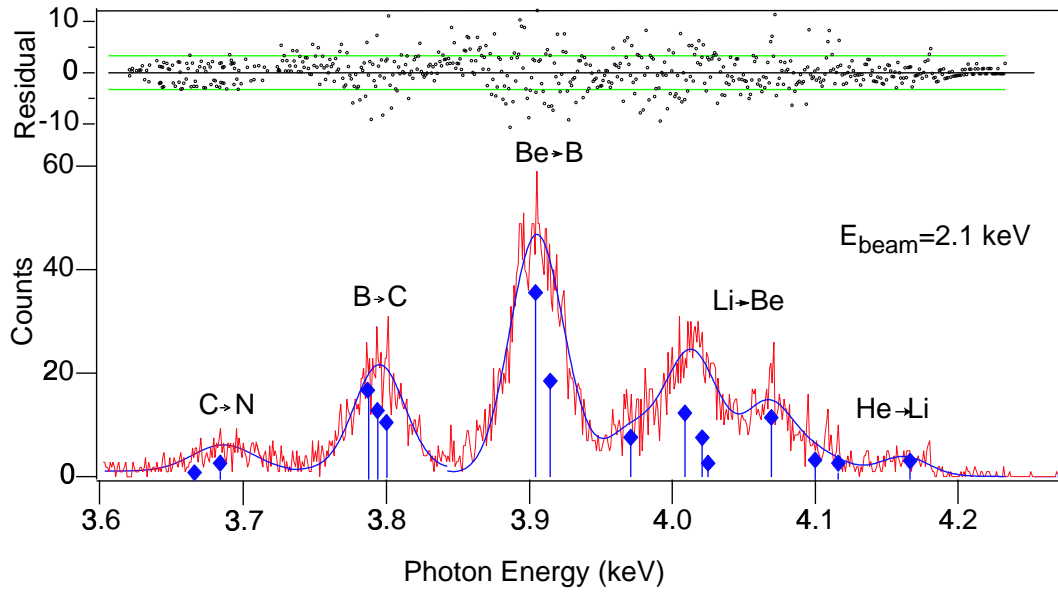


Fig. 4.— The Fe RR spectrum and a spectral fit to the data at an electron beam energy of 2.1 keV. The vertical bars with diamond tops indicate the position and intensity of individual RR lines from different charge states.

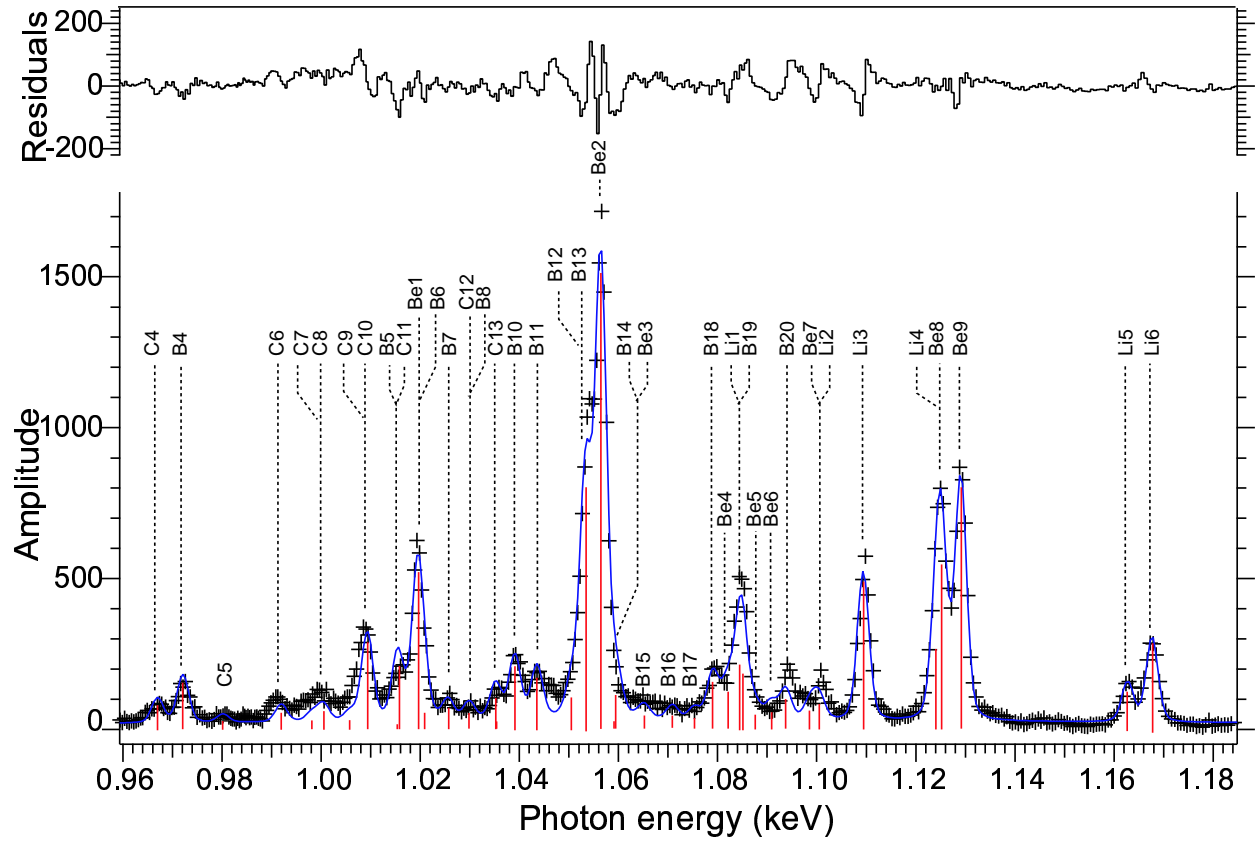


Fig. 5.— Fe crystal spectrum and its fit at an electron energy of 2.1 keV. The lines are labeled with notation by Brown et al. (2002); the transitions are listed in Table 3.

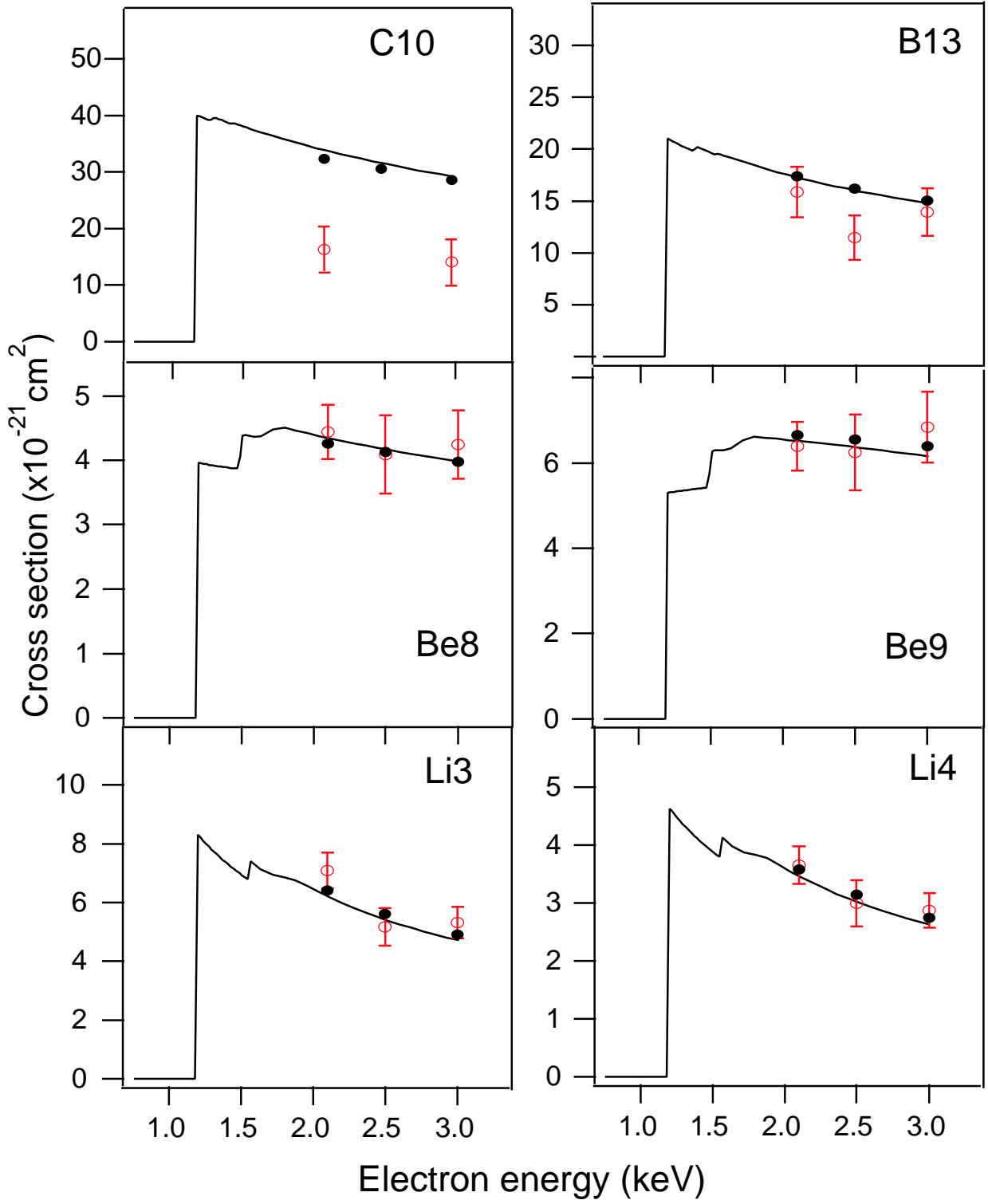


Fig. 6.— The measured effective excitation cross section (open circles with error bar) for lines from 4 different charge states and comparison with theoretical calculations using the codes HULLAC (lines) and FAC (solid circles).